

rspa.royalsocietypublishing.org

Research



**Cite this article:** Reeves-McLaren N, Sharp J, Beltrán-Mir H, Rainforth WM, West AR. 2016 Spinel–rock salt transformation in  $\text{LiCoMnO}_{4-\delta}$ . *Proc. R. Soc. A* **472**: 20140991. <http://dx.doi.org/10.1098/rspa.2014.0991>

Received: 23 December 2014

Accepted: 1 December 2015

### Subject Areas:

materials science, energy, inorganic chemistry

### Keywords:

$\text{LiCoMnO}_4$ , Rietveld, electron energy loss spectroscopy, X-ray absorption near edge structure, Raman, oxygen loss

### Author for correspondence:

Nik Reeves-McLaren

e-mail: [n.reeves@sheffield.ac.uk](mailto:n.reeves@sheffield.ac.uk)

Electronic supplementary material is available at <http://dx.doi.org/10.1098/rspa.2014.0991> or via <http://rspa.royalsocietypublishing.org>.

**THE ROYAL SOCIETY**  
PUBLISHING

# Spinel–rock salt transformation in $\text{LiCoMnO}_{4-\delta}$

Nik Reeves-McLaren<sup>1</sup>, Joanne Sharp<sup>1</sup>, Héctor Beltrán-Mir<sup>2</sup>, W. Mark Rainforth<sup>1</sup> and Anthony R. West<sup>1</sup>

<sup>1</sup>Department of Materials Science and Engineering, University of Sheffield, Sheffield S1 3JD, UK

<sup>2</sup>Departamento de Química Inorgánica y Orgánica, Universidad Jaume I, Avda. Sos Baynat s/n, Castellón 12071, Spain

The transformation on heating  $\text{LiCoMnO}_4$ , with a spinel structure, to  $\text{LiCoMnO}_3$ , with a cation-disordered rock salt structure, accompanied by loss of 25% of the oxygen, has been followed using a combination of diffraction, microscopy and spectroscopy techniques. The transformation does not proceed by a topotactic mechanism, even though the spinel and rock salt phases have a similar, cubic close-packed oxygen sublattice. Instead, the transformation passes through two stages involving, first, precipitation of  $\text{Li}_2\text{MnO}_3$ , leaving behind a Li-deficient, Co-rich non-stoichiometric spinel and, second, rehomogenization of the two-phase assemblage, accompanied by additional oxygen loss, to give the homogeneous rock salt final product; a combination of electron energy loss spectroscopy and X-ray absorption near edge structure analyses showed oxidation states of  $\text{Co}^{2+}$  and  $\text{Mn}^{3+}$  in  $\text{LiCoMnO}_3$ . Subsolvus phase diagram determination of the  $\text{Li}_2\text{O-CoO}_x\text{-MnO}_y$  system has established the compositional extent of spinel solid solutions at approximately 500°C.

## 1. Introduction

$\text{LiCoMnO}_4$  is of considerable interest as a five-volt cathode in lithium ion batteries [1–7]. However, samples are often oxygen-deficient and this introduces an additional, lower voltage redox reaction associated

© 2016 The Authors. Published by the Royal Society under the terms of the Creative Commons Attribution License <http://creativecommons.org/licenses/by/4.0/>, which permits unrestricted use, provided the original author and source are credited.

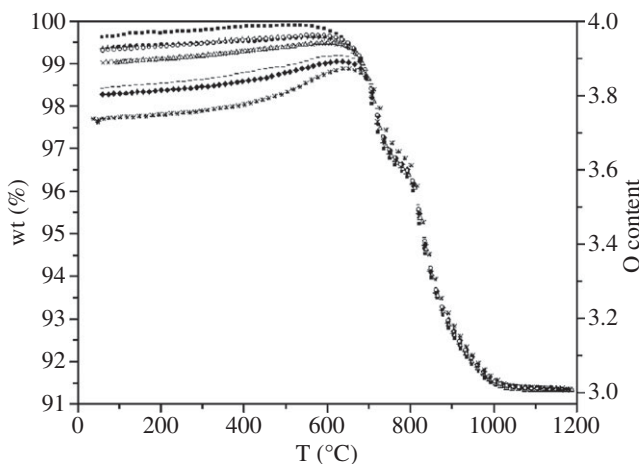


**Figure 1.** Thermogravimetric data for  $\text{LiCoMnO}_{4-\delta}$  samples, from [8].

with Li deintercalation and subsequent reintercalation, thereby affecting the performance of the material as a five-volt cathode.  $\text{LiCoMnO}_4$  loses oxygen readily on heating: thermogravimetric, TG, analysis shows loss of up to 25% of its oxygen content over the temperature range approximately 500–1050°C on heating in air (figure 1) [8]. This oxygen loss is accompanied by a transformation from the spinel structure of  $\text{LiCoMnO}_4$  to a cation-disordered rock salt structure of stoichiometry  $\text{LiCoMnO}_3$ . Our previous work [9] has shown that this weight loss is reversible on cooling, with the degree of oxygen uptake dependent on the cooling rate; even with relatively fast cooling rates of up to  $10^\circ\text{C min}^{-1}$ , a single-phase spinel was observed in diffraction data.

Both spinel and rock salt structures have a cubic close-packed oxide ion arrangement with cations distributed over various octahedral and tetrahedral sites. In spinels, the distribution of cations over interstitial sites is often described using the cation inversion parameter,  $\gamma$ :

$$\begin{aligned}\gamma = 0: & \quad [\text{A}]^{\text{tet}}[\text{B}_2]^{\text{oct}}\text{X}_4 &= \text{'normal' } \\ \gamma = 1: & \quad [\text{B}]^{\text{tet}}[\text{AB}]^{\text{oct}}\text{X}_4 &= \text{'inverse' } \\ \gamma = 0.67: & \quad [\text{B}_{0.67}\text{A}_{0.33}]^{\text{tet}}[\text{A}_{0.67}\text{B}_{1.33}]^{\text{oct}}\text{X}_4 &= \text{'random' }.\end{aligned}$$

An intriguing question concerns the mechanism by which  $\text{LiCoMnO}_4$ , a close-packed oxide, is able to lose 25% of its oxygens on heating and subsequently reincorporate them on cooling: it seems inconceivable that this could take place as a topotactic reaction in which the integrity of the spinel and rock salt lattices is retained throughout.

The main purpose of this paper is to investigate the spinel to rock salt transformation on heating. To do this, samples were quenched from different temperatures and analysed using a complementary range of diffraction, microscopic and spectroscopic techniques. Since it became apparent that the cationic compositions of the spinel and/or rock salt phases were variable during the phase transformation, a subsolidus phase diagram study was also required to determine the possible stoichiometry ranges of the various phases. In completing this study, our interest has been, first, to determine the range of compositions that form a cubic spinel structure under normal conditions of solid-state reaction and, second, to understand the products of decomposition of  $\text{LiCoMnO}_4$  at various temperatures.

Two reports [1,10] have been made previously on the phase diagram of this system, using milligram-scale specimens made via solution-based combinatorial synthesis. Samples were heated at 800°C or 900°C for 3 h and either quenched by removing from the furnace and placing on a metal slab or slow-cooled at approximately  $10^\circ\text{C min}^{-1}$  by switching off the furnace.

## 2. Experimental set-up

For initial phase diagram studies, samples were prepared using  $\text{Li}_2\text{CO}_3$  (99+%, dried at  $180^\circ\text{C}$ ),  $\text{Co}(\text{NO}_3)_2 \cdot 6\text{H}_2\text{O}$  (98+%) and  $(\text{CH}_3\text{CO}_2)_2\text{Mn} \cdot 4\text{H}_2\text{O}$  (99+%) as starting reagents (all Sigma-Aldrich). Appropriate weighed amounts were mixed with acetone in an agate mortar and pestle, dried, placed into gold boats, fired at  $650^\circ\text{C}$  for decarbonation and at  $800^\circ\text{C}$  to complete the reaction. Post-annealing was then conducted to maximize the oxygen contents by holding the specimens at  $500^\circ\text{C}$  for 3 days.

For subsequent work to prepare single-phase samples of  $\text{LiCoMnO}_4$  for phase transformation studies, a sol-gel synthesis route was devised using  $\text{LiNO}_3$  (99%),  $\text{CoCl}_2$  (99%) and  $\text{MnCl}_2$  (98%), all Strem Chemicals (Bischheim, France). First,  $\text{MnCl}_2$  was dissolved in ethanol ( $\text{EtOH}$ ) and acetylacetone ( $\text{acacH}$ ) at room temperature. The  $\text{Mn} : \text{EtOH} : \text{acacH}$  molar ratio was 1 : 20 : 6. If  $\text{MnCl}_2$  was dissolved in ethanol alone, a white suspension was observed after addition of ethanol; this precipitation was avoided by adding acetylacetone. Acetylacetone ( $\text{acacH}$ ) is a rather strong chelating ligand that has often been reported in the sol-gel literature to stabilize non-silicate metal alkoxide precursors. Complexing ligands such as  $\text{acacH}$  lead to less-hydrolysable M-acac bonds [11]. The resulting solution was stirred for 5 min and then  $\text{CoCl}_2$  and  $\text{LiNO}_3$  were added in sequence. The final mixture was stirred for 4 h and heated under reflux ( $85^\circ\text{C}$ ) for 4 days. The resulting sol led to a transparent gel after evaporation of the solvent, which became a powder after drying under an IR lamp. This powder was heated slowly to  $700^\circ\text{C}$  under flowing  $\text{O}_2$ , and maintained at  $700^\circ\text{C}$  for 48 h with intermittent regrinding using an agate mortar and pestle.

For phase transformation studies, small quantities (approx. 1 g) of this reacted powder were wrapped in Au or Pt foil, heated isothermally in a vertical tube furnace at various temperatures for 1 h, then quenched into liquid nitrogen ( $200^\circ\text{C s}^{-1}$ ) in order to preserve high-temperature phase assemblage(s) while preventing re-uptake of oxygen during cooling. These quenched specimens are referred to as Q597, Q679, Q700, Q744, Q849, Q950 and Q1048; the numbers refer to the quench temperature in degree celsius.

X-ray powder diffraction (XRD) used a STOE STADI P diffractometer,  $\text{Mo K}\alpha_1$  radiation ( $\lambda = 0.70930 \text{ \AA}$ ) with a linear position-sensitive detector for lattice parameter measurements and structure refinement. Initial data analysis used the STOE WinX<sup>POW</sup> software package. Rietveld refinement used the EXPGUI [12] interface for GSAS [13]; the errors quoted are as given by GSAS. Initial isotropic thermal parameters,  $U_{\text{iso}}$ , were  $0.025 \text{ \AA}^2$  for all positions. The total occupancy of sites was set to unity. The background and scale factors were refined first, using a shifted Chebyshev function with six terms for the background, followed by the lattice and profile parameters. Atomic positions were refined in order of scattering power. The whole process was repeated to convergence with negligible shifts in atomic variables.

Micro-X-ray absorption spectroscopy was conducted on the as-prepared material and Q679, Q700, Q744, Q849, Q950 and Q1048 at the microfocus spectroscopy beamline (I18) at the Diamond Light Source, Didcot, UK. The beam size was around  $3 \times 3 \mu\text{m}$ . Specimens were prepared by dispersion of powders in isopropanol and mounted on lacey carbon films. Elemental mapping was collected over the Co and Mn *K*-edges to check sample homogeneity, before individual spectra were collected over both *K*-edges. A 9-element Ge detector was used. Data treatment used the Athena [14] software package. Single-element distribution maps were prepared using PyMca v. 4.6.2 [15].

Raman spectra were excited with the 514.5 nm line of an Ar laser and recorded in back scattering geometry using a Renishaw inVia micro-Raman spectrometer. Laser power of approximately 2 mW was focused on an approximate  $1 \mu\text{m}$  spot. The spectrometer was equipped with a Peltier-cooled multichannel CCD detector and  $2400 \text{ l mm}^{-1}$  diffraction grating with slit opening  $65 \mu\text{m}$  and spectral resolution approximately  $1 \text{ cm}^{-1}$ . Data analysis used Igor Pro v. 6.06 [16].

Transmission electron microscopy (TEM) samples were made from as-prepared powder and samples quenched from each temperature by dispersion in isopropanol and collection on a lacey carbon film. Specimens were examined in a JEOL 2010F TEM at 200 kV using electron energy

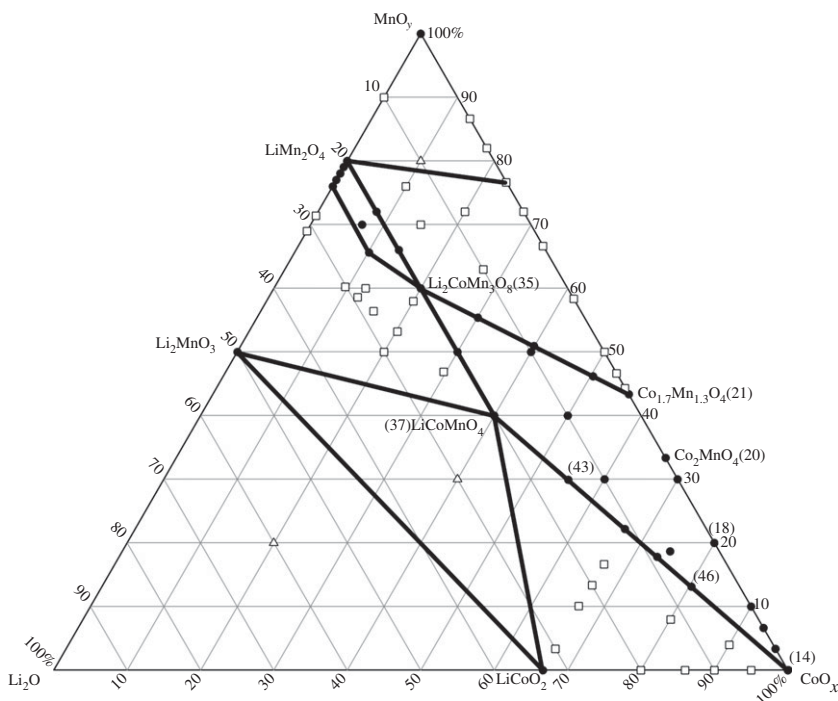


**Figure 2.** Pseudoternary subsolidus phase diagram at 500°C for the  $\text{Li}_2\text{O}-\text{CoO}_x-\text{MnO}_y$  system; solid lines indicate boundaries of compatibility regions. Selected composition numbers included for reference (see electronic supplementary material, table S1 and table 2). Circles denote single phase, squares, two phases and triangles, three phases.

loss spectroscopy (EELS) with a beam size of approximately 15 nm (EDS mode). Spectra were recorded from a number of locations with thickness 0.2–0.8 inelastic mean free paths, determined using the low-loss spectrum. Data were taken from O-K (532 eV), Mn- $L_{2,3}$  (640 eV) and Co- $L_{2,3}$  (779 eV) edges.

EELS spectra were background-subtracted using a power-law model, and plural scattering deconvoluted using the Fourier-ratio method. Mn valences were determined using the ratio between integrals under the EELS Mn- $L_3/L_2$  peaks and background-corrected using the Pearson approach [17]. Reference  $L_3/L_2$  versus valence curves were calculated from spectra taken using  $\text{MnO}_2$  ( $\text{Mn}^{4+}$ ),  $\text{Mn}_2\text{O}_3$  ( $\text{Mn}^{3+}$ ) and freshly obtained  $\text{MnO}$  ( $\text{Mn}^{2+}$ ). A programme was written using Igor to facilitate this because of the large volume of data collected. Valence determination was also attempted for Co, but was unsuccessful, giving results with error bars so large as to render the results meaningless, so is not included here.

### 3. Results

#### (a) Phase diagram studies

A number of compositions in the pseudoternary system  $\text{Li}_2\text{O}-\text{CoO}_x-\text{MnO}_y$  system were prepared and by combining these results, electronic supplementary material, table S1, with selected results from the literature, an isothermal section for samples reacted at 800°C in air and given a final annealing at 500°C was obtained and is presented in figure 2. Both Co and Mn can assume a variety of oxidation states, and, therefore, the phase diagram is not truly ternary since it includes different regions in the quaternary system Li-Co-Mn-O. Because of uncertainties in oxygen contents, the results are projected onto the pseudoternary section  $\text{Li}_2\text{O}-\text{CoO}_x-\text{MnO}_y$ ; this enables the cation contents to be specified but allows variation in the Co/Mn oxidation states.

Samples were prepared by solid-state synthesis with final reaction for 3 days at 800°C to attain thermodynamic equilibrium, followed by post-annealing at 500°C in air to maximize oxygen contents. Reaction at 800°C was chosen since samples heated at lower temperatures, or for less time, often failed to react fully, whereas heating at much higher temperatures risked significant loss of lithia and/or phase transformations associated with loss of oxygen [4,6]. The usual tests for thermodynamic equilibrium were applied, namely that, for a selection of samples, the phase or phase mixture in the products did not change on further heating at the same or slightly higher temperature.

First, we summarize results on the three binary edges and compare these with the literature. Previous reports on spinel formation in  $\text{Li}_2\text{O}-\text{MnO}_y$  compositions showed the formation of a solid solution between the binary phases  $\text{LiMn}_2\text{O}_4$  and  $\text{Li}_4\text{Mn}_5\text{O}_{12}$  [18], i.e.  $\text{Li}_{1+x}\text{Mn}_{2-x}\text{O}_{4-\delta}$ :  $0 \leq x \leq 0.33$ . In our studies, the solubility limit was found to be  $x = 0.16$  after the final heat treatment at 500°C; this is consistent with the literature since 500°C is above the decomposition temperature of the more Li-rich solid solutions in this series, including  $\text{Li}_4\text{Mn}_5\text{O}_{12}$ .

No evidence was seen for the formation of any spinel phases under our reaction conditions in  $\text{Li}_2\text{O}-\text{CoO}_x$  compositions, which is also consistent with the literature; previous studies by Levasseur *et al.* [19] found a limited range of  $\text{Li}_{1+x}\text{Co}_{1-x}\text{O}_2$  solid solutions,  $0 \leq x \leq 0.07$  formed under oxygen gas at 900°C, though no evidence for this was seen under our synthesis conditions.

A range of cubic spinel solid solutions based on  $\text{Co}_3\text{O}_4$  was found over the composition range  $\text{Co}_{3-y}\text{Mn}_y\text{O}_4$ :  $0 < y < 1.3$ , which compares reasonably well with that found by Brown *et al.* [10], with a composition limit at  $y = 1.08$ . The minor difference in extent may be due to differences in the heating/cooling regimes used and the difficulty in achieving thermodynamic equilibrium at these temperatures. This is apparent in the high-temperature phase diagram study in air of the system Co-Mn-O by Aukrust & Muan [20], where it is suggested that the compositional extent of the cubic spinel solid solution decreases with decreasing temperature, although no quantitative data were given. Compositions in the range  $1.30 < y < 2.16$  yielded a mixture of cubic and tetragonal spinels, whose compositions were assumed to be  $y = 1.30$  and 2.16, respectively, while for  $y \geq 2.30$  two-phase assemblages of tetragonal spinel and bixbyite,  $\text{Mn}_2\text{O}_3$  were obtained.

The pseudoternary phase diagram (figure 2) was constructed using the above results on the binary spinel solid solutions and those given in electronic supplementary material, table S1. It contains two large areas of cubic spinel solid solutions that broadly extend from solid solutions  $\text{Li}_{1+x}\text{Mn}_{2-x}\text{O}_4$  on the  $\text{Li}_2\text{O}-\text{Mn}-\text{O}$  edge to the  $\text{Co}_{3-y}\text{Mn}_y\text{O}_4$  solid solutions on the Co-Mn-O edge [14,15]. Within these solid solution areas, two ‘ideal’ composition ranges can be identified: first, the join between  $\text{LiMn}_2\text{O}_4$  and  $\text{LiCoMnO}_4$ , with the replacement mechanism, assuming full oxygen stoichiometry,  $\text{Mn}^{3+} = \text{Co}^{3+}$  and which also includes the composition,  $\text{Li}_2\text{CoMn}_3\text{O}_8$ ; second, the join between  $\text{Co}_3\text{O}_4$  and  $\text{LiCoMnO}_4$  with the replacement mechanism,  $\text{Co}^{2+} + \text{Co}^{3+} = \text{Li}^+ + \text{Mn}^{4+}$ . The two spinel solid solution areas are effectively separated by the composition  $\text{Li}_2\text{CoMn}_3\text{O}_8$ , figure 2. One large, quadrilateral-shaped cubic area has compositions containing less than or equal to 20 mole%  $\text{Li}_2\text{O}$  and is limited by the phase compositions:  $\text{Co}_3\text{O}_4$ ,  $\text{Co}_{1.7}\text{Mn}_{1.3}\text{O}_4$ ,  $\text{Li}_2\text{CoMn}_3\text{O}_8$  and  $\text{LiCoMnO}_4$ . Lattice parameters were refined in GSAS using Le Bail fits (table 1) for a selected number of compositions in this area; a minimum in lattice parameter occurs at  $\text{LiCoMnO}_4$ , and unit cell size increases with Co and/or Mn content to a maximum at  $\text{Co}_{1.7}\text{Mn}_{1.3}\text{O}_4$ .

The second, smaller area has compositions greater than or equal to 20 mole%  $\text{Li}_2\text{O}$  and is limited by  $\text{Li}_2\text{CoMn}_3\text{O}_8$  and  $\text{LiMn}_2\text{O}_4$  with a limited range of Li-rich solid solutions whose limit is temperature-dependent. Thus, Robertson *et al.* [21] reported low-temperature synthesis of a complete range of solid solution between  $\text{Li}_4\text{Mn}_5\text{O}_{12}$  and  $\text{LiCoMnO}_4$  of general formula  $\text{Li}_{4-x}\text{Mn}_{5-2x}\text{Co}_{3x}\text{O}_{12}$ ,  $0 \leq x \leq 1$  with a maximum synthesis temperature of 440°C, significantly lower than that used in this study. As stated above, at 500°C the  $\text{LiMn}_2\text{O}_4$  solid solutions do not extend as far as  $\text{Li}_4\text{Mn}_5\text{O}_{12}$  and, therefore, the size of these Li-rich solid solutions with more than 20%  $\text{Li}_2\text{O}$  is smaller than in the work of Robertson *et al.* [21].

The size and shape of the spinel solid solution areas shown in figure 2 are broadly similar to those reported in [1,10]. Direct comparison is difficult because of the very different synthesis

**Table 1.** Refined lattice parameter for various cubic spinel phases, and for those in  $\text{LiCoMnO}_4$  quenched from various temperatures. Composition number (see electronic supplementary material, table S1) for reference also included.

specimen (composition number)	lattice parameter (Å)
$\text{Co}_3\text{O}_4$ (14)	8.0838 (19)
$\text{Co}_{2.4}\text{Mn}_{0.6}\text{O}_4$ (18)	8.1808 (10)
$\text{Co}_2\text{MnO}_4$ (20)	8.2582 (10)
$\text{Co}_{1.7}\text{Mn}_{1.3}\text{O}_4$ (21)	8.3214 (14)
$\text{Li}_2\text{CoMn}_3\text{O}_8$ (35)	8.1316 (8)
$\text{Li}_{0.78}\text{Co}_{1.44}\text{Mn}_{0.78}\text{O}_4$ (43)	8.0665 (7)
$\text{Li}_{0.37}\text{Co}_{2.26}\text{Mn}_{0.37}\text{O}_4$ (46)	8.07629 (17)
as prepared	8.05982 (41)
Q597	8.06705 (34)
Q679	8.07912 (48)
Q700	8.09784 (48)
Q744	8.13072 (61)

conditions used. In [1,10], small samples were prepared by combinatorial synthesis, initially deposited as liquid mixtures which were dried and fired at  $800^\circ\text{C}$  or  $900^\circ\text{C}$  for 3 h. Results were very dependent on cooling conditions because oxidation was presumed to occur at slower cooling rates; the results for slow-cooled samples were most similar to those shown in figure 2, but samples were not given a prolonged anneal at  $500^\circ\text{C}$ .

The rest of the phase diagram at  $500^\circ\text{C}$  is divided into a number of two- and three-phase compatibility regions. Of these, one region bounded by  $\text{LiMn}_2\text{O}_4$ ,  $\text{Li}_2\text{CoMn}_3\text{O}_8$ ,  $\text{Co}_{1.7}\text{Mn}_{1.3}\text{O}_4$  and approximately  $\text{Co}_{0.8}\text{Mn}_{2.2}\text{O}_4$  yields a mixture of two spinel phases, one with cubic and one with tetragonal symmetry. The tetragonal spinel appears to have the composition  $\text{Co}_{0.8}\text{Mn}_{2.2}\text{O}_4$ ; the cubic spinel is the range of compositions linking  $\text{Co}_{1.7}\text{Mn}_{1.3}\text{O}_4$ ,  $\text{Li}_2\text{CoMn}_3\text{O}_8$  and  $\text{LiMn}_2\text{O}_4$ . In the  $\text{CoO}_x\text{-MnO}_y$  binary system, it has been reported [20] that compositions between  $\text{Co}_{1.7}\text{Mn}_{1.3}\text{O}_4$  and  $\text{Co}_{0.8}\text{Mn}_{2.2}\text{O}_4$  form a single-phase cubic spinel at elevated temperatures; it may be that Li-containing compositions within the ternary mixed-phase region also follow this behaviour but are beyond the scope of this study.

Samples prepared within the region bounded by  $\text{LiMn}_2\text{O}_4$ ,  $\text{MnO}_y$  and approximately  $\text{Co}_{0.8}\text{Mn}_{2.2}\text{O}_4$  yielded a mixture of cubic spinel ( $\text{LiMn}_2\text{O}_4$ ), tetragonal spinel and bixbyite ( $\text{Mn}_2\text{O}_3$ ). The tetragonal spinel and bixbyite phases may exist over limited composition ranges, as reported in [1,10].

The join  $\text{LiCoO}_2\text{-Li}_2\text{MnO}_3$  has been extensively studied because of its relevance to lithium battery cathodes. For instance, McCalla *et al.* [1] reported the formation of a complete series of rock salt-related solid solutions in quenched samples, but which were found to phase separate during slow cooling. The endpoints of this coexistence after phase separation were not stoichiometric  $\text{LiCoO}_2$  and  $\text{Li}_2\text{MnO}_3$ ; instead,  $\text{LiCoO}_2$  contained some Mn and  $\text{Li}_2\text{MnO}_{3-\delta}$  contained some Co; similar conclusions were reported in [1]. Consistent with these studies, we note the existence of a three-phase compatibility triangle at  $500^\circ\text{C}$  bounded by  $\text{LiCoO}_2$ ,  $\text{Li}_2\text{MnO}_3$  and  $\text{LiCoMnO}_4$  (figure 2).

## (b) Powder X-ray diffraction studies of $\text{LiCoMnO}_{4-\delta}$

A specimen of  $\text{LiCoMnO}_4$  was synthesized via the sol-gel route using a final heat treatment at  $700^\circ\text{C}$  under flowing oxygen as outlined above. It was then slow-cooled to room temperature, in order to maximize oxygen content: the TG data in figure 1 show that oxygen loss in



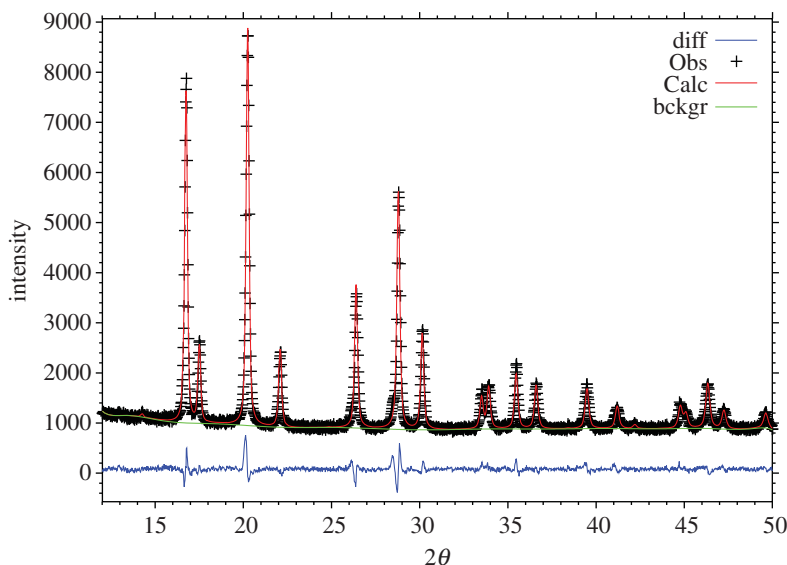


**Figure 3.** Observed, calculated and difference profiles from XRD data for  $\text{LiCoMnO}_4$  at room temperature. (Online version in colour.)

$\text{LiCoMnO}_{4-\delta}$  is continuous with temperature over the range approximately 600–1000°C, but there is also evidence that it occurs in two stages with a poorly resolved intermediate plateau at approximately 775°C.

From powder XRD data, all reflections were indexed using the spinel space group,  $\text{Fd}\bar{3}\text{m}$ ,  $a = 8.05982(4) \text{ \AA}$ , and so, by XRD, the specimen appeared to be single phase. The crystal structure was confirmed using Rietveld refinement to be a normal spinel; Li occupies the  $8a$  tetrahedral site, Co and Mn share the  $16d$  octahedral site, and oxygen occupies the  $32e$  site. After simultaneous refinement of all appropriate parameters, the visual fit of the data (figure 3) was good, as were the quality indicators:  $\chi^2 = 2.140$ ,  $R_{\text{wp}} = 4.24\%$  and  $R_p = 3.13\%$ . The isotropic thermal parameters were acceptable for all sites; final refined structural parameters are given in table 2.

XRD data collected from quenched samples showed a complex series of changes on heating (figure 4*a*). Phase-pure cubic spinel structure was retained in Q597. Data for Q679 indicated that decomposition had begun with the appearance of  $\text{Li}_2\text{MnO}_3$ . Although the main (001) reflection for this layered rock salt overlaps with the spinel (111) reflection at  $ca\ 8.7^\circ 2\theta$ , the (020) and (110) reflections from the layered rock salt phase are diagnostic, first appear for Q679 and increase in intensity with quench temperature, as shown at 700°C, 744°C and 849°C (figure 4*b*). In Q849, peaks from a third phase with a disordered rock salt XRD pattern were observed (figure 4*a*). Q950 showed mainly the disordered rock salt phase, with a small spinel peak at approximately  $16^\circ 2\theta$ ; Q1048 was phase-pure disordered rock salt. At this temperature, TG data (figure 1) show that 25% of the oxygen content has been lost giving a rock salt stoichiometry ' $\text{LiCoMnO}_3$ '.

Lattice parameters of the spinel phase in quenched samples (table 1) show a nonlinear increase with quench temperature. There are two possible causes of this, both of which would be consistent with our results. First, oxygen loss may cause a reduction in oxidation state of Co and/or Mn. Second, the spinel phase may become richer in Co, consequent upon precipitation of  $\text{Li}_2\text{MnO}_3$ .

As well as the various phase changes observed on heating, changes in certain line intensities of the spinel phase occurred, particularly the (220) peak at approximately  $14^\circ 2\theta$  (figure 4*a,b*). For cubic spinels, the (220) line in XRD data is especially sensitive to the occupancy of the  $8a$  tetrahedral site. If the spinel is fully normal and Li occupies the  $8a$  site, this line should be effectively absent; however, if cation mixing occurs, with a heavier scatterer (e.g. Co and/or Mn)

**Table 2.** Structure refinement parameters and bond lengths for LiCoMnO<sub>4</sub> at room temperature.

parameter	value
space group	Fd $\bar{3}$ m
$a$ (Å)	8.05982 (41)
$V$ (Å <sup>3</sup> )	523.57 (8)
$\chi$	2.140
$R_{wp}$ (%)	4.24
$R_p$ (%)	3.13
cation site	8a
$x(=y=z)$	0.125
site occupancy	1.0 Li
$U_{iso}$ (Å <sup>2</sup> )	0.0116 (43)
cation site	16d
$x(=y=z)$	0.5
site occupancy	0.5 Co/0.5 Mn
$U_{iso}$ (Å <sup>2</sup> )	0.0004 (4)
oxygen site	32e
$x(=y=z)$	0.26145 (26)
site occupancy	1.0 O
$U_{iso}$ (Å <sup>2</sup> )	0.0028 (8)
bond lengths (Å)	
Li-O	1.904(1) $\times$ 4
(Co,Mn)-O	1.927(1) $\times$ 6

on this site, then the line intensity should increase. Such behaviour is readily apparent in figure 4b, suggesting that cation mixing on the 8a site occurs during heating.

An analysis of intensity ratios for the spinel (111) and (311) lines provides a further sensitive indicator of cation distribution. In as-prepared LiCoMnO<sub>4</sub>, this ratio was 1.37 compared to 0.12 for Co<sub>3</sub>O<sub>4</sub> and 0.10 for Co<sub>2</sub>MnO<sub>4</sub>. This ratio remained constant, within reasonable errors, for Q597, Q679 and Q700, but decreased to 1.01 for Q744 and 0.26 for Q849. This decrease is further evidence for increased occupancy of the 8a sites by Co/Mn and is consistent with the spinel phase becoming increasingly Li-deficient on heating, as a consequence of decomposition of the original LiCoMnO<sub>4</sub> into Li<sub>2</sub>MnO<sub>3</sub>- and Co<sub>2</sub>MnO<sub>4</sub>-like phases.

Results on the high-temperature decomposition of LiCoMnO<sub>4</sub> can be interpreted qualitatively in terms of the phase diagram (figure 2) although the diagram refers to equilibration at 500°C. The appearance of Li<sub>2</sub>MnO<sub>3</sub> at intermediate temperatures indicates that the spinel becomes Li-deficient and, indeed, may lie on a line passing through Li<sub>2</sub>MnO<sub>3</sub> and LiCoMnO<sub>4</sub> and towards, but not extending as far as, Co<sub>2</sub>MnO<sub>4</sub>. This is supported by changes in XRD intensities of the spinel referred to above and is further supported by separate observations that synthesis of phase-pure LiCoMnO<sub>4</sub> requires a final anneal at low temperatures in order to both optimize oxygen content and prevent formation of Li<sub>2</sub>MnO<sub>3</sub> [5–7,22].

At the highest temperatures studied, a disordered rock salt phase appears and is phase-pure at 1048°C. From TG results (figure 1) LiCoMnO<sub>4</sub> has lost up to 25% of its oxygen at these temperatures and therefore the rock salt phase has the overall stoichiometry LiCoMnO<sub>3</sub>. It is well known that under appropriate conditions of low oxygen partial pressure, CoO and MnO have



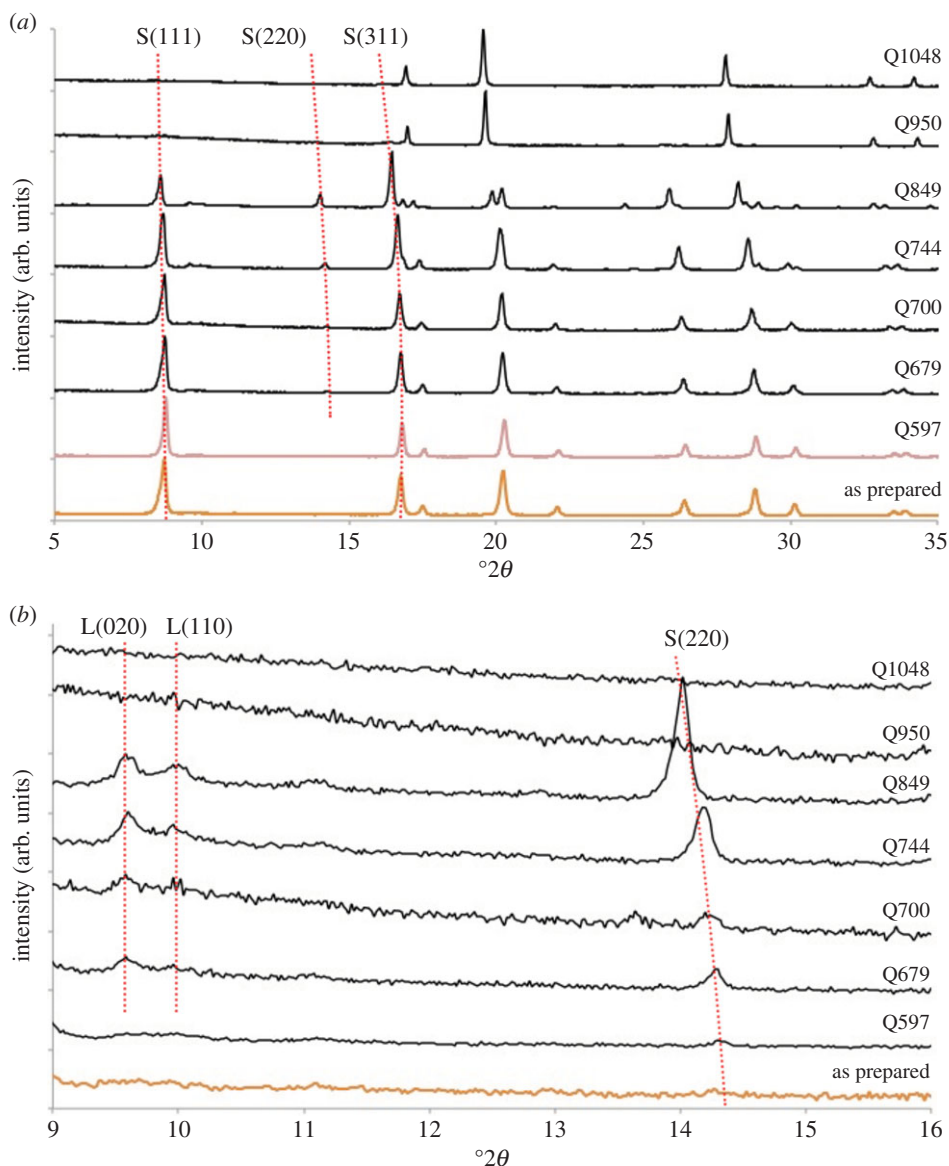


**Figure 4.** (a) X-ray diffraction patterns for as-prepared and quenched specimens of  $\text{LiCoMnO}_4$  and (b) expanded view to show  $\text{Li}_2\text{MnO}_3$  peaks, L(110), L(020) and growth of S(220) spinel line with quench temperature. (Online version in colour.)

the rock salt structure; both  $\text{LiCoO}_2$  and  $\text{Li}_2\text{MnO}_3$  have ordered rock salt structures but appear not to disorder prior to melting. We may therefore add the composition  $\text{LiCoMnO}_3$  to the list of phases that exhibit a high-temperature rock salt structure and also speculate that a large area(s) of compositions in the pseudoternary system  $\text{Li}_2\text{O-Mn-Co-O}$ , with appropriate adjustment of their oxygen contents, may exist with the cation-disordered rock salt structure.

### (c) X-ray absorption near edge spectroscopy

The homogeneity of as-prepared  $\text{LiCoMnO}_4$  was checked initially using maps of X-ray absorption (figure 5) collected at the Mn and Co K-edge energy levels in raster fashion across a sample that had an area including multiple grains. Essentially, brighter colours indicate a greater concentration of that element. Each pixel on the maps refers to a  $5 \times 5 \mu\text{m}$  area spot size. On

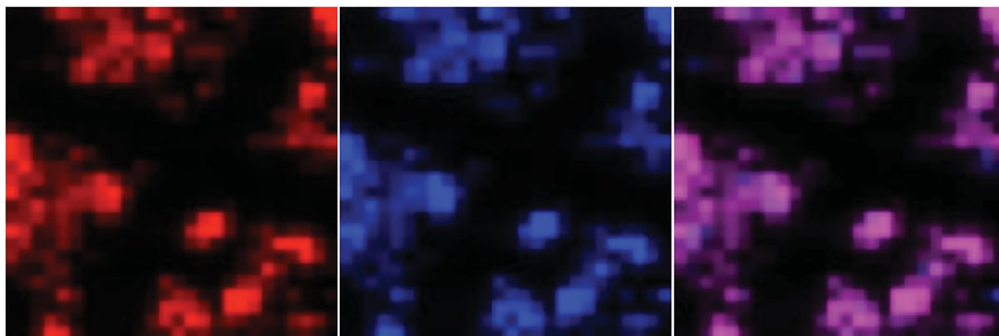


**Figure 5.** Colour-coded single-element distribution maps for Mn (red), Co (blue) and Mn, Co together, for as-prepared  $\text{LiCoMnO}_4$ .

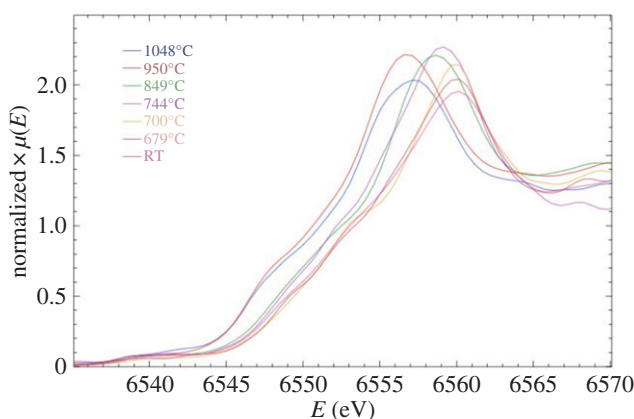


**Figure 6.** Mn  $K$ -edge XANES spectra for  $\text{LiCoMnO}_4$  quenched from various temperatures.

combining Mn (figure 5a) and Co (figure 5b) maps to form the overall map in figure 5c, any areas lacking in either element should be readily apparent; the general lack of red or blue ‘pixels’ on the combined map indicates a reasonable level of metal homogeneity on this length scale.

Mn and Co  $K$ -edge spectra for  $\text{LiCoMnO}_4$  quenched from different temperatures are shown in figures 6 and 7. Standard samples containing known valences of Mn and Co were also measured (not shown). In order to extract valence state information from the spectra of quenched samples, the maxima of their absorption edges were compared with those of the standards, as summarized in figure 8 and table 3. The as-prepared sample and specimens quenched from 679°C, 700°C and 744°C gave Mn  $K$ -edge maxima that matched well with that of the  $\text{Mn}^{4+}$  reference. In samples quenched from higher temperatures,  $E_0$  shifted to lower energies (figure 6) corresponding to a decrease in average Mn oxidation state, over micrometre length scales. Samples quenched from 950°C and 1048°C gave edge maxima close to that observed for the  $\text{Mn}^{3+}$  reference (figure 8).

For the Co  $K$ -edge spectra, a reasonable match in edge position was found for  $\text{LiCo}^{3+}\text{O}_2$ , the as-prepared specimen and those quenched from 679°C and 700°C. The edge position moved to lower energies with increasing quench temperature (figure 7) corresponding to a reduction in the average oxidation state from  $\text{Co}^{3+}$  to almost  $\text{Co}^{2+}$  (table 3 and figure 8).

The interpretation of these XANES data is that in  $\text{LiCoMnO}_4$ , Co and Mn are essentially in +3 and +4 oxidation states, respectively. The Co oxidation state might be slightly less than +3 if the  $\text{LiCoMnO}_4$  were slightly oxygen-deficient: the sample was not heated in high pressure oxygen as part of the post-reaction anneal. With the onset of oxygen loss on heating, the Co

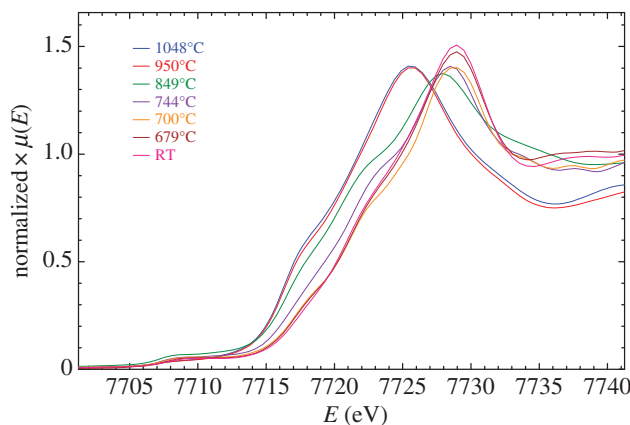


**Figure 7.** Co K-edge XANES spectra for  $\text{LiCoMnO}_4$  quenched from various temperatures.

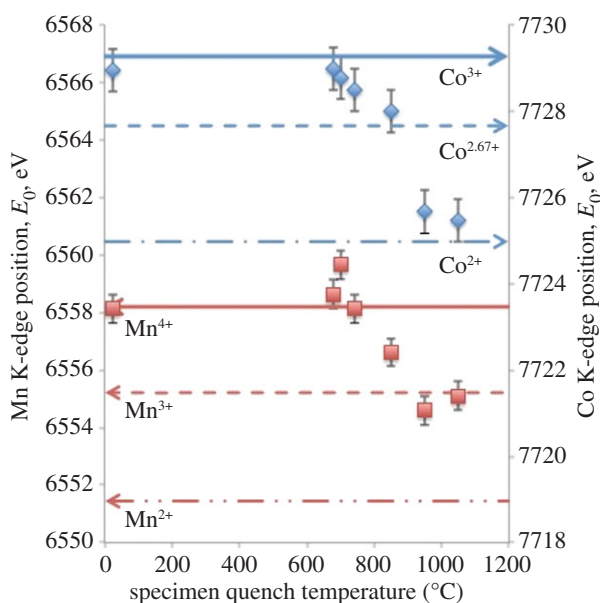


**Figure 8.** Determination of average Mn and Co valence states from XANES data of as-prepared and quenched  $\text{LiCoMnO}_4$  using calibration peak maximum values measured from standard materials:  $\text{C}_4\text{H}_6\text{Mn}^{2+}\text{O}_4 \cdot 4\text{H}_2\text{O}$  (red dotted dashed line),  $\text{Mn}_2^{3+}\text{O}_3$  (red dashes) and  $\text{Mn}^{4+}\text{O}_2$  (red solid line),  $\text{Co}^{2+}\text{O}$  (blue dotted dashed line),  $\text{Co}_3^{2.67+}\text{O}_4$  (blue dashes) and  $\text{LiCo}^{3+}\text{O}_2$  (blue solid line).

oxidation state starts to reduce (figure 8) at a lower temperature,  $690 \pm 30^\circ\text{C}$ , than reduction of the Mn oxidation state,  $800 \pm 55^\circ\text{C}$ ; therefore, the initial oxygen loss appears to be charge-compensated by reduction of the Co valence state. At temperatures where  $\text{Li}_2\text{MnO}_3$  appears as a secondary phase,  $744^\circ\text{C}$  and  $849^\circ\text{C}$ , the Mn oxidation state starts to reduce; as there is little evidence of significant oxygen loss from  $\text{Li}_2\text{MnO}_3$  [23], it appears that Mn in the spinel phase starts to reduce at  $849^\circ\text{C}$ , whereas the Co valence state is already clearly a mixture of 2+ and 3+ at these temperatures. At the highest temperatures,  $950^\circ\text{C}$  and  $1048^\circ\text{C}$ , where the structures are cation-disordered, phase-pure rock salt, the valence states are  $\text{Co}^{2+}$  and  $\text{Mn}^{3+}$ , consistent with the general formula  $\text{LiCo}^{2+}\text{Mn}^{3+}\text{O}_3$ .

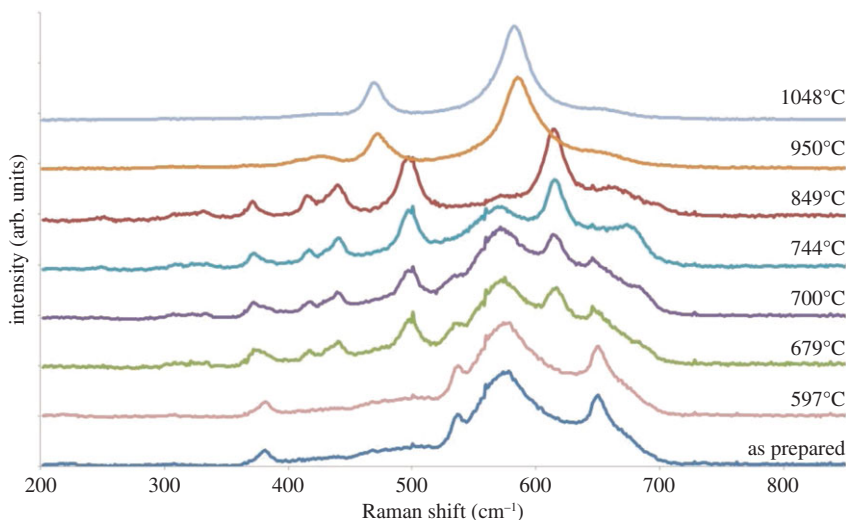


**Figure 9.** Raman spectra for as-prepared and quenched  $\text{LiCoMnO}_4$ . (Online version in colour.)

**Table 3.** Mn and Co  $K$ -edge positions for reference standard materials and as-prepared and quenched  $\text{LiCoMnO}_4$  specimens. Errors in  $E_0$  estimated at the size of one data point,  $\pm 0.5$  eV.

Mn $K$ -edge		Co $K$ -edge	
reference materials	$E_0$ (eV)	reference materials	$E_0$ (eV)
$\text{C}_4\text{H}_6\text{Mn}^{2+}\text{O}_{4.4}\text{H}_2\text{O}$	6551.4	$\text{Co}^{2+}\text{O}$	7725.0
$\text{Mn}_2^{3+}\text{O}_3$	6555.2	$\text{Co}_3^{2.67+}\text{O}_4$	7727.7
$\text{Mn}^{4+}\text{O}_2$	6558.2	$\text{LiCo}^{3+}\text{O}_2$	7729.3
LiCoMnO <sub>4-<math>\delta</math></sub> specimens			
quench temperature ( $^{\circ}\text{C}$ )	$E_0$ (eV)	$E_0$ (eV)	
as prepared	6558.1	7729.0	
679	6558.6	7729.0	
700	6559.7	7728.8	
744	6558.1	7728.5	
849	6556.6	7728.0	
950	6554.6	7725.7	
1048	6555.1	7725.5	

#### (d) Raman spectroscopy

Raman spectra (figure 9) for as-prepared and quenched  $\text{LiCoMnO}_4$  powders can be divided into three groups:

- Spectra of as-prepared powder and that quenched from  $597^{\circ}\text{C}$  are similar to that reported previously by Dokko *et al.* [24] and show four broad lines at  $652$ ,  $581$ ,  $539$  and  $384\text{ cm}^{-1}$ , which can be attributed to  $A_{1g}$ ,  $F_{2g}^{(1)}$ ,  $F_{2g}^{(2)}$  and either  $E_g$  or  $F_{2g}^{(3)}$  modes, respectively [24–28]. An additional line seen by Dokko *et al.* at  $692\text{ cm}^{-1}$ , and attributed to the presence of  $\text{Co}_3\text{O}_4$  was not observed here.

- (ii) Specimens quenched from 679, 700, 744 and 849°C retain these four spectral lines, but also exhibit four new lines at *ca* 619, 501, 445 and 420 cm<sup>-1</sup> which match those of Li<sub>2</sub>MnO<sub>3</sub> [29]. The lines of both spinel and layered rock salt phases shift to slightly lower wavenumbers with increasing quench temperature and the intensities of the spinel lines diminish on further heating.
- (iii) Specimens quenched from 950 and 1048°C showed only two broad lines, at *ca* 476 and 588 cm<sup>-1</sup>, which we attribute to modes from a disordered rock salt phase, consistent with similar spectra reported for CoO [30,31].

In conclusion, the Raman results agree with those obtained by XRD concerning the sequence of phase changes and the temperatures over which they occur.

### (e) Transmission electron microscopy

TEM images are shown in figure 10; three broad regimes of particle morphology can be observed. First, in the as-prepared specimen and those quenched from 700°C and below, TEM images showed slightly faceted crystallites with an approximate average diameter of 100 nm. Second, more strongly faceted crystallites were observed in Q744 and, with a roughly fourfold increase in size in Q849.

Third, in Q1048 much larger, rounded particles were observed, with size of approximately 1 µm. For Q950, two distinct populations were observed, with a mixture of both rounded and faceted particles. Preparation of suitably thin specimens for TEM analysis was difficult for specimens quenched from 950°C and 1048°C, as these also showed a tendency to form agglomerates.

### (f) Electron energy loss spectroscopy

EELS analyses were conducted on the Mn-*L*<sub>2,3</sub>, Co-*L*<sub>2,3</sub> and O-K edges. For each sample, multiple points were analysed across several grains that were thin enough for study.

In the low-temperature parent phase, LiCoMnO<sub>4</sub>, the O-K edge is characteristic of a spinel-type oxygen lattice, whereas in specimens quenched from higher temperatures, O-K edges resemble those of rock salt-type oxygen lattices [32]. Examples of these two extremes are shown in figure 11. Between these extremes, intermediate O-K edge shapes and positions were found; typical examples are given in figure 12. Least-squares fitting of the intermediate O-K edge to a mixture of rock salt and spinel edges yielded results with high  $\chi^2$ -values. This indicates that the two-phase composite structure is more complex than simple, side-by-side coexistence of discrete spinel and rock salt regions within the illuminated sample volume.

One possibility is that the pre-peak seen in the spinel edge is a sign of oxygen loss caused by beam damage, as reported for some other oxides [33]; in this event, the pre-peak should grow and subsequently shrink, as described in [17], during beam exposure. This possibility was tested, but the intensity of the pre-peak relative to the rest of the O-K edge remained unchanged; instead, the whole edge decreased in intensity on prolonged exposure, after which a hole was observed in the sample. The pre-peak is, therefore, a genuine feature of the sample; perhaps, the lattice itself has an inhomogeneous distribution of O vacancies, for example.

Mn-*L*<sub>2,3</sub> edges from each quench temperature are shown in figure 13. Mn oxidation states were derived from *L*<sub>3</sub>/*L*<sub>2</sub> peak ratio analysis. The derived oxidation states are lower than those found from XANES data, indicating there are likely to be systematic errors in the absolute values. This is probably related to (i) the analysis coming only from the edges of the grains where they were thin enough for EELS analysis and/or (ii) the limited number of standard data points used to construct the Mn oxidation state reference curve, leading to a displacement in the reference curve's position. The shape of this reference curve is less in question, however, so the positions of derived Mn oxidation states relative to each other and, in conjunction with the O-K edge analyses,

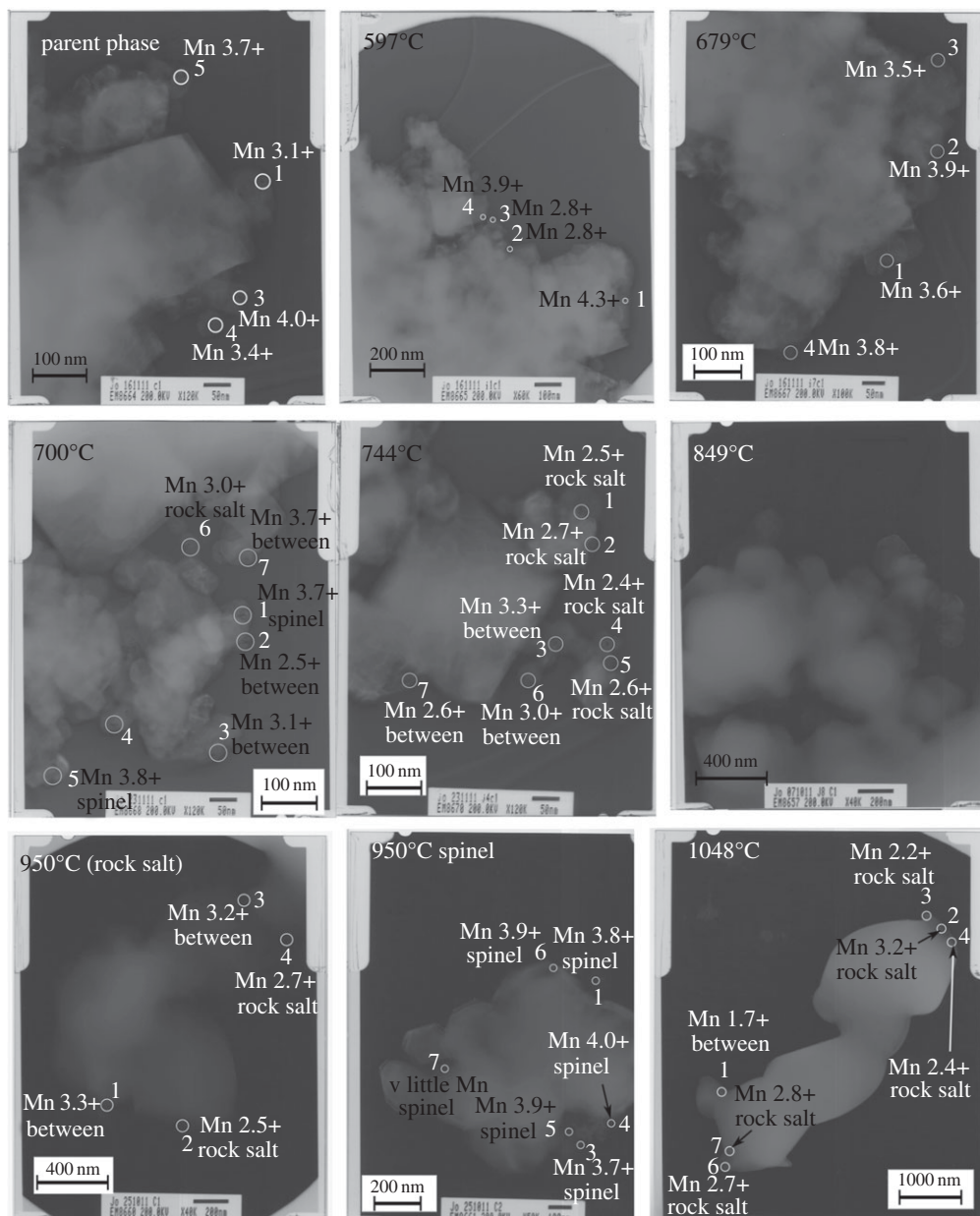


**Figure 10.** TEM images from quenched samples.

are instructive. Consequently, the Mn oxidation states and O-K edges from EELS can be assigned to three general regimes (figure 14).

First, spinel-like materials were observed for as-prepared  $\text{LiCoMnO}_4$ , Q597, Q679 and Q700.  $L_3/L_2$  peak ratios gave average Mn oxidation states of approximately 3.9+, with the exception of Q700, where an average of  $\text{Mn}^{3.73+}$  was calculated.

Second, very small inclusions of layered rock-salt  $\text{Li}_2\text{MnO}_3$  were found under most conditions, including in the as-prepared material. In each case, the average Mn oxidation state calculated from  $L_3/L_2$  peak ratios was around 3.2+. The exceptions were Q597 and Q1048. This implies that the parent phase may locally have oxygen-deficient regions and associated  $\text{Li}_2\text{MnO}_3$ -type inclusions which were annealed out on heating at approximately 597°C and no longer present at 1048°C.



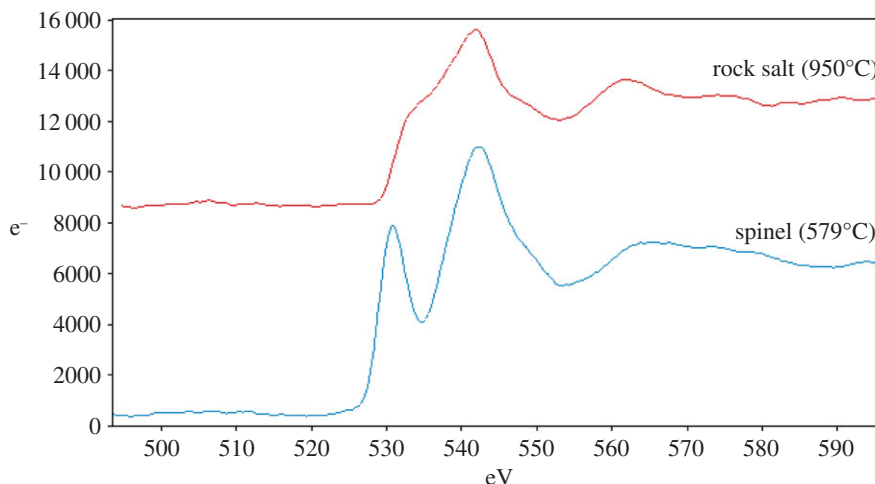


**Figure 11.** O K EELS edges from cubic spinel  $\text{LiCoMnO}_4$  (Q597), and disordered rock salt (Q950). (Online version in colour.)

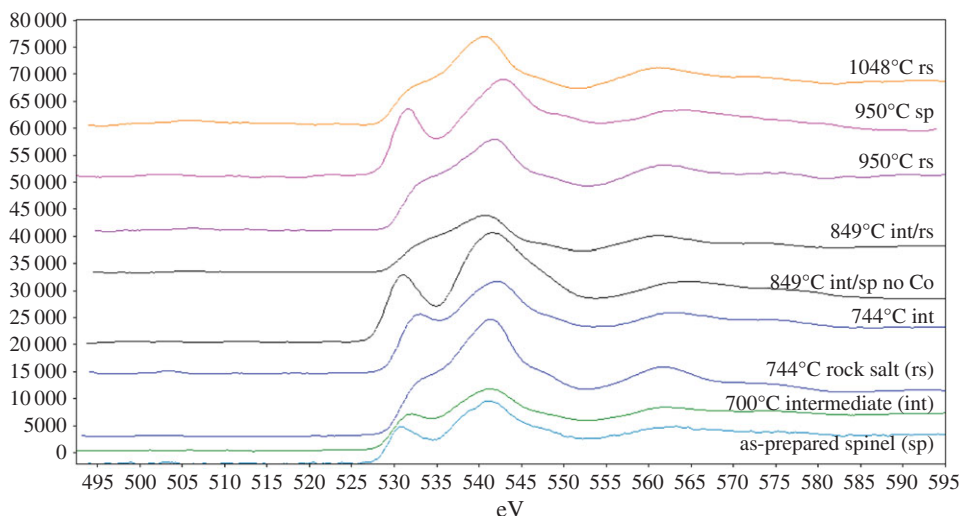


**Figure 12.** O K edges from different quench temperatures, scaled and offset to fit on the same axes. Labelling shows attribution of edge to spinel (sp), rock salt (rs) or intermediate (int) regions. (Online version in colour.)

Finally, O-K edges indicative of rock salt lattices were observed in all specimens quenched from 700°C or higher. The average Mn oxidation state decreased with increasing quench temperature, from 3.1+ in Q700 to 1.8+ in Q1048 (as mentioned previously in this section, absolute values have systematic errors but relative values are reliable).

The observed Co- $L_{2,3}$  edges are presented in figure 15. The signal : noise ratio is significantly poorer at this higher energy loss and, therefore, there is more error in the calculated oxidation states. We were unable to observe any statistically significant changes in Co  $L$ -edge shapes or positions with quench temperature and, as a result, there was minimal sensitivity to the changes in oxidation state expected in these samples. Nevertheless, the presence or the absence of Co  $L$ -edge peaks could at least be used to analyse local Co distributions in grains of different phases throughout the specimen. Co was found in all three (spinel, layered rock-salt and disordered rock salt) phases in specimens collected from all temperatures, though some particles that did not show a Co edge in EELS analysis, mainly from 849°C, were also observed.

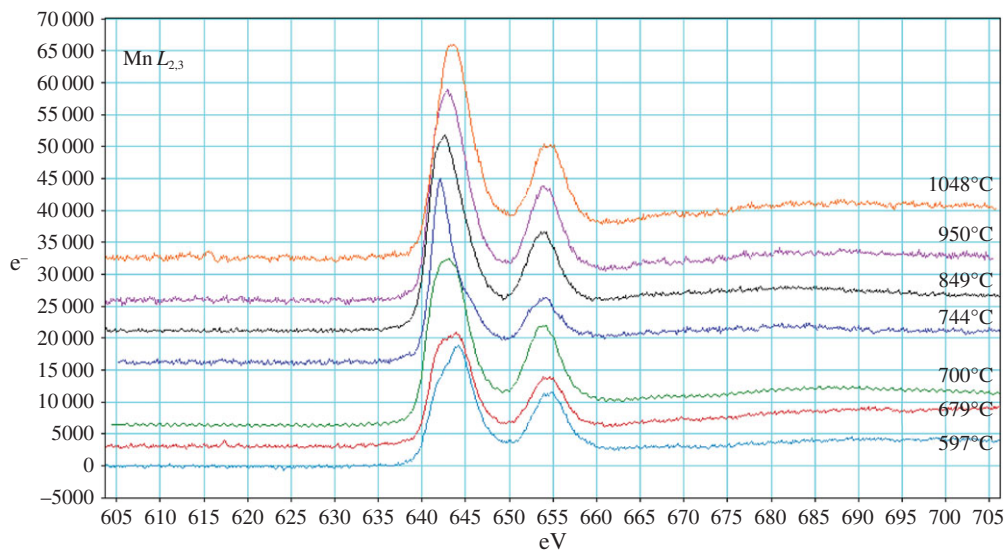


**Figure 13.** Mn  $L_{2,3}$  edges from material quenched at different temperatures, offset and scaled to fit on same axes. (Online version in colour.)

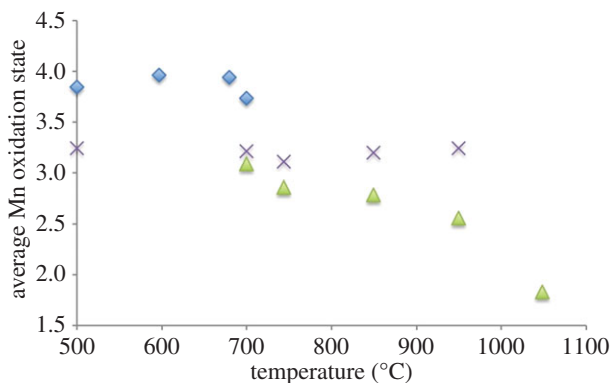


**Figure 14.** Averaged Mn oxidation state obtained from EELS data differentiated by  $O K$  edge shape and position (blue diamonds, spinel; purple crosses,  $\text{Li}_2\text{MnO}_3$ ; green triangles, disordered rock salt). (Online version in colour.)

## 4. Discussion

The combination of techniques that probe structure/composition over different length scales gives a good picture of the difficulty in preparing single-phase homogeneous ceramic powders of  $\text{LiCoMnO}_4$ , despite (i) the use of sol-gel techniques to promote homogenization of the reaction product and (ii) reaction in an oxygen atmosphere to ensure maximum reaction without oxygen loss.

XRD data on as-prepared specimens showed that single-phase  $\text{LiCoMnO}_4$  was obtained. Data from micrometre-scale probes—Raman spectroscopy and XANES—are in good agreement with the XRD analysis; in particular, no evidence of any secondary phases was found via Raman spectra collected from various spots. However, the nano-scale EELS technique showed inhomogeneities in thinner parts of TEM specimens and regions in which the Mn oxidation state is reduced to below four, possibly due to the loss of oxygen from sample surfaces.

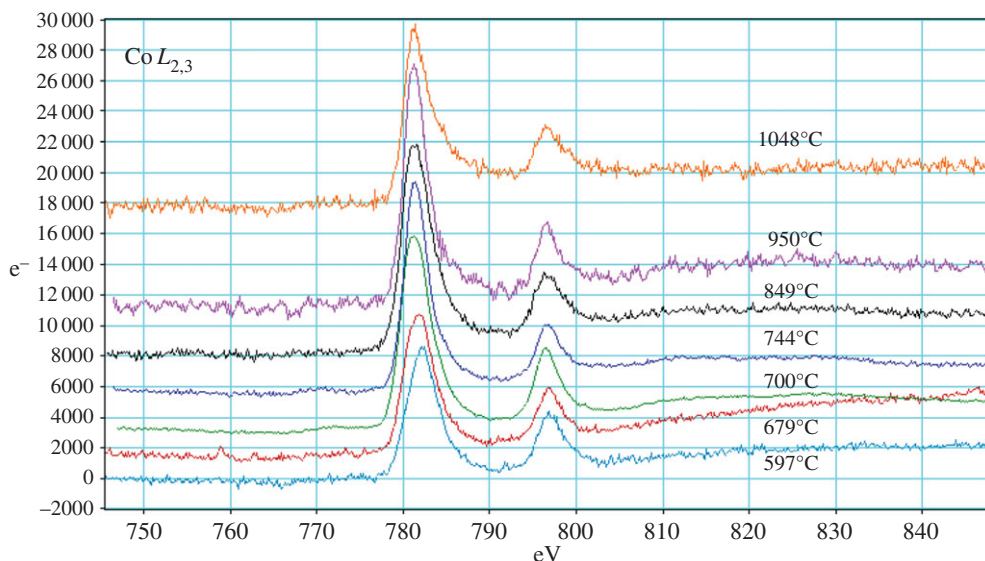
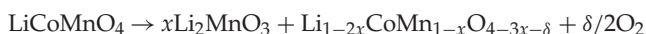


**Figure 15.** Top:  $\text{Co } L_{2,3}$  edges from different temperatures, offset and scaled to fit on axes. (Online version in colour.)

The results obtained from the combination of characterization techniques show that, on heating, weight loss from  $\text{LiCoMnO}_4$  proceeds in essentially three stages:

- (i) A drop in oxygen content commences approximately above  $600^\circ\text{C}$ , associated primarily with reduction of Co and segregation of  $\text{Li}_2\text{MnO}_3$ . It is not known how much oxygen loss can be tolerated by  $\text{LiCoMnO}_4$  prior to precipitation of  $\text{Li}_2\text{MnO}_3$  due to the relative insensitivity of the bulk phase analysis techniques, XRD and Raman spectroscopy, to small amounts of secondary phases, but there is clear evidence of precipitation of  $\text{Li}_2\text{MnO}_3$  by  $679^\circ\text{C}$ . From consideration of the phase diagram, it is reasonable to assume that the spinel phase therefore becomes increasingly Li-deficient following the general reaction:



- (ii) We do not know if the  $\text{Li}_2\text{MnO}_3$  precipitate is stoichiometric, contains a small amount of Co, or is slightly oxygen-deficient.
- (iii) A short intermediate weight loss ‘plateau’ occurs at approximately  $780^\circ\text{C}$ , where the rate of oxygen loss slows; the overall oxygen content is approximately 3.67. If the lithium-deficient spinel phase has retained a cation: oxygen ratio of 3:4, then  $\delta = x$ , giving  $x \approx 0.33$ . The spinel composition at  $780^\circ\text{C}$  would, therefore, be close to  $\text{Li}_{0.33}\text{CoMn}_{0.67}\text{O}_{2.67}$  (i.e.  $\text{Li}_{0.5}\text{Co}_{1.5}\text{MnO}_4$  or  $\text{Li}(\text{Co}_3\text{Mn}_2)\text{O}_8$ ), which is similar to other known spinel phases such as  $\text{LiFe}_5\text{O}_8$  and  $\text{LiAl}_5\text{O}_8$ .
- (iv) Oxygen loss continues on further heating above  $800^\circ\text{C}$ , as the intermediate phases recombine to yield a single-phase, disordered rock salt structure by approximately  $1000^\circ\text{C}$ . Thus, the intermediate spinel phase,  $\text{LiCo}_3\text{Mn}_2\text{O}_8$ , loses more oxygen and cation homogenization occurs with the overall reaction:



The driving force for oxygen loss on heating  $\text{LiCoMnO}_4$  may, therefore, be the precipitation of  $\text{Li}_2\text{MnO}_3$  which, compared to spinel, is effectively oxygen-deficient. It may be that significant oxygen deficiency does not exist in  $\text{LiCoMnO}_4$  as previously suggested, but

rather than  $\text{LiCoMnO}_4$  simply has an upper limit of stability, and on heating above  $600^\circ\text{C}$  it shows retrograde solubility to give a precipitate of  $\text{Li}_2\text{MnO}_3$  and a non-stoichiometric, Li-deficient spinel.

## 5. Conclusion

The fundamental question concerning the mechanism by which  $\text{LiCoMnO}_4$  spinel transforms to  $\text{LiCoMnO}_3$  with a cation-disordered rock salt structure has been resolved. It is not a topotactic reaction involving reversible loss and subsequent uptake of 25% of the oxide ions from the cubic close-packed oxygen sublattice. Instead, in the first stage,  $\text{LiCoMnO}_4$  becomes a supersaturated solid solution on heating and precipitates  $\text{Li}_2\text{MnO}_3$  together with associated oxygen loss. At the same time, the spinel host structure becomes Li-deficient, with an increased Co:Mn ratio and a composition that approximates to  $\text{Li}_{0.5}\text{Co}_{1.5}\text{MnO}_4$ .

In the second stage,  $\text{Li}_2\text{MnO}_3$  and  $\text{Li}_{0.5}\text{Co}_{1.5}\text{MnO}_4$  re-react, with further oxygen loss from the spinel component, to give a cation-disordered rock salt phase,  $\text{LiCoMnO}_3$ . Hence, the final product,  $\text{LiCoMnO}_3$ , has the same cation composition as the  $\text{LiCoMnO}_4$  starting phase but with 25% less oxygen; the transformation passes through an intermediate two-phase equilibrium assemblage in which the cationic compositions of the two phases are very different and probably temperature-dependent. The overall mechanism therefore involves cation segregation and subsequent rehomogenization at the same time as oxygen loss occurs. TEM studies show significant changes in particle size and shape, indicating nucleation and growth mechanisms for the different stages. A homogeneous topotactic phase transformation does not occur.

**Data accessibility.** Supporting data are available on request via email from the corresponding author.

**Authors' contributions.** N.R.-M., A.R.W., J.S., H.B.M. all made substantial contributions to conception and design, syntheses of specimens, acquisition of data, and/or analysis and interpretation of data. W.M.R. was involved with drafting the article or revising it critically for important intellectual content, and interpretation of TEM and EELS data. All named authors were involved and gave final approval.

**Competing interests.** We have no competing interests.

**Funding.** This work was fully funded solely by EPSRC.

**Acknowledgements.** We thank the EPSRC for financial support, and Diamond Beamline I18 Senior Support Scientist Tina Geraki for assistance and useful discussions.

## References

- McCalla E, Lowartz CM, Brown CR, Dahn JR. 2013 Formation of layered–layered composites in the Li–Co–Mn oxide pseudoternary system during slow cooling. *Chem. Mater.* **25**, 912–918. (doi:10.1021/cm304002b)
- Huang X, Lin M, Tong Q, Li X, Ruan Y, Yang Y. 2012 Synthesis of  $\text{LiCoMnO}_4$  via a sol–gel method and its application in high power  $\text{LiCoMnO}_4/\text{Li}_4\text{Ti}_5\text{O}_{12}$  lithium-ion batteries. *J. Power Sources* **202**, 352–356. (doi:10.1016/j.jpowsour.2011.11.028)
- Strobel P, Tillier J, Diaz A, Ibarra-Palos A, Thiéry F, Soupart JB. 2007 Search for new manganese–cobalt oxides as positive electrode materials for lithium batteries. *J. Power Sources* **174**, 910–915. (doi:10.1016/j.jpowsour.2007.06.080)
- Zhecheva E, Stoyanova R, Alcántara R, Lavela P, Tirado JL. 2006 EPR studies of Li deintercalation from  $\text{LiCoMnO}_4$  spinel-type electrode active material. *J. Power Sources* **159**, 1389–1394. (doi:10.1016/j.jpowsour.2005.11.088)
- West AR, Kawai H, Kageyama H, Tabuchi M, Nagata M, Tukamoto H. 2001 Electrochemical, electrical and magnetic properties and valence state distributions in the high voltage spinel cathode solid solutions  $\text{Li}_{1-x}\text{Co}_{1/2+3x/3}\text{Mn}_{3/2-x/2}\text{O}_4$ :  $-0.33 \leq x \leq 1$ . *J. Mater. Chem.* **11**, 1662–1670. (doi:10.1039/b101788h)
- Kawai H, Nagata M, Tukamoto H, West AR. 1999 High-voltage lithium cathode materials. *J. Power Sources* **81–82**, 67–72. (doi:10.1016/S0378-7753(98)00204-3)
- Kawai H, Nagata M, Kageyama H, Tukamoto H, West AR. 1999 5 V lithium cathodes based on spinel solid solutions  $\text{Li}_2\text{Co}_{1+x}\text{Mn}_{3-x}\text{O}_8$ :  $-1 \leq X \leq 1$ . *Electrochim. Acta* **45**, 315–327. (doi:10.1016/S0013-4686(99)00213-3)

8. Pasero D, de Souza S, Reeves N, West AR. 2005 Oxygen content and electrochemical activity of  $\text{LiCoMnO}_{4-\delta}$ . *J. Mater. Chem.* **15**, 4435–4440. (doi:10.1039/b508521g)
9. Reeves N, Kirk CA, West AR. 2001 Reversible spinel to rock salt transition in  $\text{LiCoMnO}_d$  by oxygen (de) intercalation. *J. Mater. Chem.* **11**, 249–250. (doi:10.1039/b007595g)
10. Brown CR, McCalla E, Dahn JR. 2013 Analysis of the cubic spinel region of the Li–Co–Mn oxide pseudo-ternary system. *Solid State Ionics* **253**, 234–238. (doi:10.1016/j.ssi.2013.09.051)
11. Sanchez C, Ribot F. 1994 Design of hybrid organic-inorganic materials synthesized via sol-gel chemistry. *New J. Chem.* **18**, 1007.
12. Toby BH. 2001 EXPGUI, a graphical user interface for GSAS. *J. Appl. Crystallogr.* **34**, 210–213. (doi:10.1107/S0021889801002242)
13. Larson AC, Von Dreele RB. 2000 General structure analysis system (GSAS). Los Alamos National Laboratory Report LAUR 86–748.
14. Ravel B, Newville M. 2005 ATHENA, ARTEMIS, HEPHAESTUS: data analysis for X-ray absorption spectroscopy using IFEFFIT. *J. Synchrotron Radiat.* **12**, 537–541. (doi:10.1107/S0909049505012719)
15. Solé VA, Paipillon E, Cotte M, Walter P, Susini J. 2007 A multiplatform code for the analysis of energy-dispersive X-ray fluorescence spectra. *Spectrochim. Acta Part B* **62**, 63–68. (doi:10.1016/j.sab.2006.12.002)
16. WaveMetrics I. Igor Pro v. 6.00. Lake Oswego, OR, USA.
17. Riedl T, Gemming T, Wetzig K. 2006 Extraction of EELS white-line intensities of manganese compounds: methods, accuracy, and valence sensitivity. *Ultramicroscopy* **106**, 284–291. (doi:10.1016/j.ultramic.2005.09.002)
18. Thackeray MM, Mansuetto MF, Dees DW, Vissers DR. 1996 The thermal stability of lithium-manganese-oxide spinel phases. *Mat. Res. Bull.* **31**, 133–140. (doi:10.1016/0025-5408(95)00190-5)
19. Levasseur S, Ménétrier M, Suard E, Delmas C. 2000 Evidence for structural defects in non-stoichiometric HT- $\text{LiCoO}_2$ : electrochemical, electronic properties and  $^7\text{Li}$  NMR studies. *Solid State Ionics* **128**, 11–24. (doi:10.1016/S0167-2738(99)00335-5)
20. Aukrust E, Muan A. 1963 Phase relations in the system cobalt oxide–manganese oxide in air. *J. Am. Ceram. Soc.* **46**, 511. (doi:10.1111/j.1151-2916.1963.tb13790.x)
21. Robertson AD, Armstrong AR, Bruce PG. 2001 Low temperature lithium manganese cobalt oxide spinels,  $\text{Li}_{4-x}\text{Mn}_{5-2x}\text{Co}_x\text{O}_{12}$  ( $0 \leq x \leq 1$ ) for use as cathode materials in rechargeable lithium batteries. *J Power Sources* **97–98**, 332–335. (doi:10.1016/S0378-7753(01)00628-0)
22. Fang H, Wang Z, Zhang B, Li X, Li G. 2007 High performance  $\text{LiNi}_{0.5}\text{Mn}_{1.5}\text{O}_4$  cathode materials synthesized by a combinational annealing method. *Electrochem. Commun.* **9**, 1077–1082. (doi:10.1016/j.elecom.2006.12.013)
23. Pasero D, McLaren V, de Souza S, West AR. 2004 Oxygen nonstoichiometry in  $\text{Li}_2\text{MnO}_3$ : an alternative explanation for its anomalous electrochemical activity. *Chem. Mater.* **17**, 345–348. (doi:10.1021/cm040186r)
24. Dokko K, Anzue N, Mohamedi M, Itoh T. 2004 Uchida I. Raman spectro-electrochemistry of  $\text{LiCo}_x\text{Mn}_{2-x}\text{O}_4$  thin film electrodes for 5 V lithium batteries. *Electrochem. Commun.* **6**, 384–388. (doi:10.1016/j.elecom.2004.02.005)
25. Wei Y, Nam KW, Kim KB, Chen G. 2006 Spectroscopic studies of the structural properties of Ni substituted spinel  $\text{LiMn}_2\text{O}_4$ . *Solid State Ionics* **177**, 29–35. (doi:10.1016/j.ssi.2005.10.015)
26. Julien CM, Massot M. 2003 Lattice vibrations of materials for lithium rechargeable batteries I. Lithium manganese oxide spinel. *Mater. Sci. Eng. B* **97**, 217–230. (doi:10.1016/S0921-5107(02)00582-2)
27. Verble JL. 1974 Temperature-dependent light-scattering studies of the Verwey transition and electronic disorder in magnetite. *Phys. Rev. B* **9**, 5236–5248. (doi:10.1103/PhysRevB.9.5236)
28. White WB, DeAngelis BA. 1967 Interpretation of the vibrational spectra of spinels. *Spectrochim. Acta Part B* **23**, 985–995. (doi:10.1016/0584-8539(67)80023-0)
29. Julien CM, Massot M. 2003 Lattice vibrations of materials for lithium rechargeable batteries III. Lithium manganese oxides. *Mater. Sci. Eng. B* **100**, 69–78. (doi:10.1016/S0921-5107(03)00077-1)
30. Choi HC, Jung YM, Noda I, Kim SB. 2003 A study of the mechanism of the electrochemical reaction of lithium with CoO by two-dimensional soft X-ray absorption spectroscopy (2D

- XAS), 2D Raman, and 2D heterospectral XAS-Raman correlation analysis. *J. Phys. Chem. B* **107**, 5806–5811. (doi:10.1021/jp030438w)
31. Tang CW, Wang CB, Chien SH. 2008 Characterization of cobalt oxides studied by FT-IR, Raman, TPR and TG-MS. *Thermochim. Acta* **473**, 68–73. (doi:10.1016/j.tca.2008.04.015)
32. Zhang Z. 2007 Surface effects in the energy loss near edge structure of different cobalt oxides. *Ultramicroscopy* **107**, 598–603. (doi:10.1016/j.ultramic.2006.11.006)
33. Jiang N, Spence JCH. 2006 Interpretation of oxygen K pre-edge peak in complex oxides. *Ultramicroscopy* **106**, 215–219. (doi:10.1016/j.ultramic.2005.07.004)